A refined Monte Carlo code for low-energy electron emission from gold material irradiated with sub-keV electrons

Liheng Zhou[1], Shuiyan Cao[2*], Tao Sun[1], Yunlong Wang[1], Jun Ma[1,3]*

Affiliations:

[1]Department of Materials Science and Technology, Nanjing University of Aeronautics and Astronautics, Nanjing 211106, China

[2]College of Physics, MIIT Key Laboratory of Aerospace Information Materials and Physics, Nanjing University of Aeronautics and Astronautics, Nanjing, 211106, China

[3]School of Nuclear Science and Technology, University of Science and Technology of China, Hefei, Anhui 230026, China.

*Corresponding author. *E-mail address:* shuiyancao@nuaa.edu.cn, junma@nuaa.edu.cn

Abstract: Considering the significance of low-energy electrons (LEEs; 0–20 eV) in radiobiology, the sensitization potential of gold nanoparticles (AuNPs) as high-flux LEE emitters when irradiated with sub-keV electrons has been suggested. In this study, a track-structure Monte Carlo simulation code using the dielectric theory was developed to simulate the transport of electrons below 50 keV in gold. In this code, modifications, particularly for elastic scattering, are implemented for a more precise description of the LEE emission in secondary electron emission. This code was validated using the secondary electron yield and backscattering coefficient. To ensure dosimetry accuracy, we further verified the code for energy deposition calculations using the Monte Carlo toolkit, Geant4. The development of this code provides a basis for future studies regarding the role of AuNPs in targeted radionuclide radiotherapy.

Keywords: Monte Carlo code, Secondary electron emission, Low-energy electrons

1 Introduction:

The higher radiobiological significance of medium-energy (< 100 keV) and low-energy (< 20 eV) electrons (LEEs) compared to the commonly used high-energy (> 100 keV) electrons has been recently emphasized in radiotherapy. These medium-energy electrons, particularly the sub-keV Auger electrons (20–500 eV), are deposited across a subcellular (< 0.5 μm) range in tissue[1] and exhibit a higher linear energy transfer (LET: 4–26 keV/μm[2]) and larger relative biological effectiveness (RBE: 1–20[3]) than commonly used ~MeV X/γ-rays (LET: 0.2–2 keV/μm, RBE: 1) in radiotherapy. Thus, similar to heavy-charged particles, this type of electron can induce extreme toxicity in small tumors, clusters of cells, or micrometastases. They also have significant potential for highly targeted implant radiation therapy[4]; however, this is only possible if they are located sufficiently close to the cell nucleus or membrane. More importantly, these nearly non-ionizing LEEs are generally considered

less important in radiology owing to the ionization potential (11.7 eV[5]) of liquid water. Following the pioneering work by Sanche *et al.*[6], several studies[7, 8] have shown that ultralow-energy electrons (LEEs or quasi-free electrons (e_{qf}^-): 0–20 eV) can increase the yield of DNA strand breaks. Although certain LEEs are unable to ionize molecules, they can still cause DNA cleavage, such as single-strand breaks (SSBs) and double-strand breaks (DSBs) with a high cross section, via dissociative electron attachment[9]. Therefore, a precise description of medium-energy electrons and LEE transport in certain biological systems is critical.

In targeted radionuclide therapy, radiolabeled high-Z nanoparticles, particularly gold nanoparticles (AuNPs), increase the absorbed dose in the near region and enhance the emission of LEEs through interactions with 10–200 keV photons and ~MeV electrons[10-13]. Unfortunately, external beams in radiotherapy, such as photons and electrons, do not penetrate biological tissues beyond the mm and cm scales, respectively[10, 14, 15]. This limits the applicability of AuNPs in localized nanoscale radiotherapy. To address this problem, an Auger electron source attached to the AuNPs has been suggested[16] to produce a larger quantity of secondary LEEs from their interactions with gold. These LEEs would have shorter ranges than the initial Auger electrons and further localize radiation energy within approximately 1–10 nm[17, 18]. Nevertheless, the influence of AuNPs irradiated with these medium- and low-energy Auger electrons has been rarely studied, and the accuracy of such studies cannot be guaranteed. A recent study[19] found that a stable monolayer film of ^{125}I on gold-coated mica substrates amplifies the LEE emission by six times. Owing to the abundant Auger electrons emitted from the decay of ^{125}I (23.0 Auger electrons per decay with an average energy of 0.5 keV[20]) bombarding the gold surface, the increase in LEEs was attributed to the secondary electron emission (SEE) from the metal. Previous SEE experiments with a gold foil have shown that primary electrons of 500–750 eV generate the highest secondary electron yield (SEY; the number of true secondary electrons (0–50 eV) emitted per incident electron) of approximately 1.2–1.7[21-23]. Based on these experiments, the potential of LEE therapy combining Auger electron emitters with AuNPs has been suggested[16]. Therefore, the primary aim of this study is to build a Monte Carlo simulation code for the transport of sub-keV electrons and LEEs in gold.

In conventional Monte Carlo simulations, electron transportation is processed through the so-called condensed history method, including multiple scattering, single scattering, and continuous

slowing down approximation (CSDA) strategies[24]. These strategies are effective and fast in macroscopic situations, yet not detailed in describing low-energy electrons owing to the neglect of the actual electron energy loss in inelastic collisions. More accurate techniques such as energy straggling strategy[24] in material science or track structure strategy[25] for microdosimetry have been developed. These methods require a detailed description of each electron interaction and considers the discrete energy loss during electron transport. There have been various well-developed generic Monte Carlo toolkits, such as Geant4[26], MCNP[27], JMCT[28], SuperMC[29], and EGSnrc[30], which are suitable for the simulation of many particles. However, most generic Monte Carlo codes use the condensed history method rather than the track-structure method. Recently, track-structure tools or codes, such as Geant4-DNA[31-34], NOREC[35], KURBUC[36], and PARTRAC[37] have been implemented to simulate discrete electron transport in liquid water down to several eV. Sakata *et al.* developed two discrete models called Geant4_DNA_Au_2016[38] and Geant4_DNA_Au_2018[39] for electron transport in gold down to 10 eV. An extension of Geant4 MicroElec was also recently developed for microdosimetry and SEE simulations in various materials[40]. He *et al.*[41] developed a Monte Carlo code for low-energy incident electron transport (down to 50 eV) in Al, Ti, Pt, or Au and adopted two strategies, namely, the CSDA and track structure. Nevertheless, to study LEE emission from the AuNP surface, Monte Carlo codes considering both LEE emission from the gold surface and the dosimetry accuracy in gold material are essential but remain lacking.

Accordingly, a refined Monte Carlo simulation code for the sub-keV electron transport in nanoscale gold material was developed. This study aims to simulate LEE emission from gold material when irradiated with sub-keV electrons. This would be beneficial for future research regarding the use of AuNPs in targeted radionuclide therapy. In this study, we demonstrate the simulation structure and discuss the physical mechanism and refinements in detail. A truncation method of the elastic cross sections is implemented by considering the Mott theory and electron-acoustic phonon scattering theory. In the inelastic calculations, the exchange effect, Born correction, and relativistic effects are simultaneously considered. The initial energy of the Fermi electrons in the conduction band electron excitation was also refined from the Fermi energy to the sampled energy from the joint density of states. The simulated SEE and calculated energy deposition were used to evaluate the reliability of the developed code for low-energy levels and the accuracy of the LEE emission and dosimetry

calculations in future studies.

2 Experimental

The present Monte Carlo code was built for low-energy electron simulations in gold using the energy straggling strategy[24]. A comprehensive process for the strategy is described by Tang *et al.*[42]. This method considers the specific electron interactions and individual energy loss in each inelastic event, which increases the accuracy of the secondary electron yield and energy distribution calculation. The low energy limit of the developed code was 0.5 eV above the Fermi level (5.53 eV) of gold. Moreover, bremsstrahlung was not considered, and the reasonably high-energy limit of the code is 100 keV. The basic structure of the simulation is illustrated in **Fig.** 1a. All formulae below are expressed in atomic units.

2.1 Elastic Scattering

The elastic scattering between the incident electrons and the strong nuclear Coulomb field represents the main cause of the angular deflection in the electron trajectory. Owing to the large mass of the nucleus compared to that of the electrons, the energy transfer of electrons during elastic scattering is negligible. In this study, the electron elastic total cross sections and differential cross sections were calculated based on the Mott theory[43] using the ELSEPA code developed by Salvat *et al.*[44, 45]. The muffin-tin radius (1.44 Å) of gold was also considered in the calculation for solid gold. In the latest version of ELSEPA[45], this low-energy limit was extended down to 5 eV. The modification of elastic scattering was introduced by the following electron-acoustic phonon scattering.
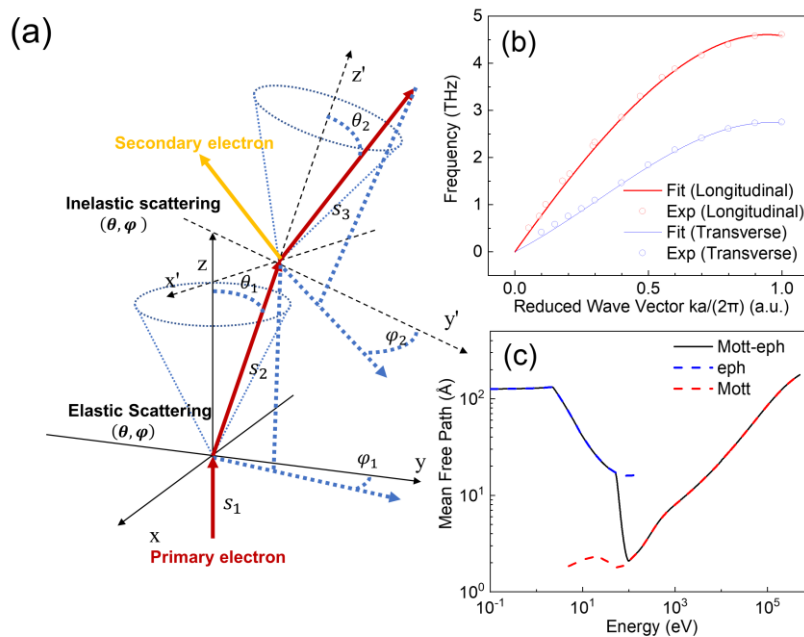
Fig. 1 a Schematic diagram of the simulation structure. **b** Phonon dispersion relations (longitudinal and transverse mode) for Au (circles represent experimental data)[46]. **c** New elastic mean free path (Mott-eph) interpolated from the Mott cross sections and electron-phonon cross sections

At very low energies, electrons tend to behave like Bloch waves rather than as particles[47]. Thus, they can interact with the collective movement of atoms in a solid, that is, phonons. We applied the theory for electron-acoustic electron scattering described by Fitting *et al.*[48] and modified by Verduin[49] and Theulings[50]. The electron-acoustic phonon scattering rate is given as follows:

$$
P_{ac}(E) = \begin{cases} \dfrac{\pi \epsilon_{ac}^2 k_B T}{\hbar c_s^2 \rho_m} \dfrac{A}{A+E} D(E), & E < \dfrac{E_{BZ}}{4} \\ \dfrac{4\pi (2N_{BZ}+1) m_D \epsilon_{ac}^2}{\hbar \omega_{BZ} \hbar \rho_m} \dfrac{A^2}{E} \left[\ln\left(\dfrac{A+E}{A}\right) - \dfrac{A}{A+E} \right], & E \geq E_{BZ} \end{cases}, \tag{1}
$$

where ϵ_{ac} is the acoustic deformation potential, k_B is the Boltzmann constant, T is the temperature, c_s is the sound velocity, ρ_m is the mass density, and $A = 5E_{BZ}$ is the screening factor adopted by Bradford and Woolf[51]. The variable E_{BZ} is the Brillouin zone energy given by $E_{BZ} = \frac{(\hbar k_{BZ})^2}{2m_e}$, where the boundary wave vector is found at $k_{BZ} = 2\pi/a$ if the first Brillouin zone is assumed to be spherical. On the other hand, a is the lattice constant, and $D(E)$ is the density of states (DOS), which is typically assumed to have a parabolic dispersion relation. In this case, $D(E)$ is expressed as follows:

$$
D(E) = \frac{\sqrt{2m_D^3 (E - E_{CB})}}{\pi^2 \hbar^3}, \tag{2}
$$

where m_D is the effective DOS mass and E_{CB} is the energy at the bottom of the conduction band and is equal to 0 for metals.

N_{BZ} is the acoustic phonon population $N(k,T)$ at the Brillouin zone boundary (k = k_{BZ}). The acoustic phonon population $N(k,T)$ follows the Bose-Einstein distribution. Thus,

$$
N(k,T) = \frac{1}{\exp\left(\frac{\hbar \omega_{ac}(k)}{k_B T}\right) - 1}, \tag{3}
$$

where ω_{BZ} is the acoustic phonon energy $\omega_{ac}(k)$ at the Brillouin-zone boundary. The acoustic phonon energy $\omega_{ac}(k)$ follows a dispersion relation that was modified to fit the experimental data[46] as follows:

$$
\omega_{ac}(k) = c_s k - \alpha k^2 - \beta k^3, \tag{4}
$$

where α and β are the fitting parameters. There are three acoustic phonon modes: one longitudinal and two transverse. For the longitudinal mode, the chosen parameters are $c_s = 3240\,\text{m/s}$, $\alpha = 3.5\times10^{-8}\,\text{m}^2/\text{s}$, and $\beta = 3.5\times10^{-18}\,\text{m}^3/\text{s}$. On the other hand, the chosen parameters for the transverse modes are $c_s = 1200\,\text{m/s}$, $\alpha = -7.6\times10^{-8}\,\text{m}^2/\text{s}$, and $\beta = 5.3\times10^{-18}\,\text{m}^3/\text{s}$. The fitted phonon dispersion relations are demonstrated in **Fig.** 1b.

Subsequently, the inverse mean free path (MFP) or macroscopic cross section can be derived by dividing the scattering rate by the electron velocity, which can be expressed as

$$\lambda_{ac}^{-1}(E) = \begin{cases} \lambda_0^{-1}\dfrac{A}{A+E}, & \text{E} < \dfrac{E_{BZ}}{4} \\ \lambda_0^{-1}\left(N_{BZ}+\dfrac{1}{2}\right)\dfrac{8m_Dc_s^2A}{\hbar\omega_{BZ}k_BT}\left[\dfrac{A}{E}\ln\left(\dfrac{A+E}{A}\right)-\dfrac{A}{A+E}\right], & \text{E} \geq \text{E}_{BZ} \end{cases}, \tag{5}$$

where $\lambda_0^{-1} = \dfrac{\sqrt{m_e^*m_D^3\epsilon_{ac}^2k_BT}}{\pi\hbar^4c_s^2\rho_m}$.

In region $[E_{BZ}/4\,, E_{BZ}]$, the inverse MFP is interpolated between both values at the upper limit of the top formula and the lower limit of the bottom formula. According to the angular differential scattering rate, the angular differential inverse MFP is given by

$$\frac{\mathrm{d}\lambda_{ac}^{-1}(E)}{\mathrm{d}\Omega} = \begin{cases} \dfrac{\lambda_0^{-1}}{4\pi}\dfrac{1}{\left(1+\frac{1-\cos\theta}{2}\frac{E}{A}\right)^2}, & \text{E} < \dfrac{E_{BZ}}{4} \\ \dfrac{\lambda_0^{-1}}{4\pi}\left(N_{BZ}+\dfrac{1}{2}\right)\dfrac{8m_Dc_s^2A}{\hbar\omega_{BZ}k_BT}\dfrac{\frac{1-\cos\theta}{2}\frac{E}{A}}{\left(1+\frac{1-\cos\theta}{2}\frac{E}{A}\right)^2}, & \text{E} \geq \text{E}_{BZ} \end{cases}. \tag{6}$$

The angular distribution of electron-acoustic scattering can also be obtained from the equation above.

Both acoustic phonon emission and absorption exist in electron-acoustic scattering; however, the probability of the former is larger than that of the latter. Therefore, the weighted average energy loss is primarily considered. Although the energy loss is only a few meV, it cannot be neglected in low-energy regions. Thus, the average energy loss E_{ac} during electron-acoustic phonon scattering can be approximated by the following expression:

$$E_{ac} = \frac{\int_0^{k_{BZ}}\hbar\omega_{ac}(k)k^2\mathrm{d}k}{\int_0^{k_{BZ}}[2N(k,T)+1]k^2\mathrm{d}k}. \tag{7}$$

Finally, the acoustic deformation potential of the metal was derived using the resistivity based on the model of Kieft and Bosch[52]. The acoustic deformation potential can then be derived as follows:

$$\epsilon_{ac} = \sqrt{\frac{2\hbar e^2 c_s^2}{3\pi m_e k_B T}\rho_R \rho_m E_F}, \tag{8}$$

where ρ_R is the resistivity. Using the parameters indicated above, the acoustic deformation potential of gold was found to be 4.86 eV and 1.80 eV for the longitudinal and transverse modes, respectively.

As suggested by Fitting *et al.*[47, 52], electrons should behave like Bloch waves and interact with phonons at low energies (< 100 eV); however, Mott cross sections are no longer valid because the unrealistically high scattering rate leads to a MFP that is shorter than the interatomic distance. Therefore, we modified the elastic scattering as follows: Mott cross sections were applied for energies above 100 eV, whereas electron-acoustic phonon cross sections were used for energies below 50 eV. The elastic cross sections between 50 eV and 100 eV were derived through interpolation between the two cross sections. As a result, a new elastic MFP is demonstrated in **Fig.** 1c. Although the elastic scattering models may not be sufficient for describing the structure of small AuNPs, a more precise atomic potential for the Mott theory will be obtained in the future using more advanced techniques, such as ab initio and DFT.

2.2 Inelastic Scattering

This study mainly considers electron-electron inelastic scattering. Inelastic cross sections were computed using the dielectric theory[53]. The core of this theory is the complex dielectric function $\varepsilon(q, \omega)$, where q is the momentum loss and ω is the energy loss. The imaginary part of the inverse dielectric function is called the energy loss function (ELF) $\mathrm{Im}\left[\frac{-1}{\varepsilon(q,\omega)}\right]$, which provides detailed energy loss information for the material electrons. From the optical data of experiments[54] or ab initio and DFT calculations[55], the dielectric function and ELF can only be obtained at the optical limit ($q \to 0$), which is called the optical dielectric function and optical ELF.

To extend the ELF from the optical limit to $q > 0$, we used the extended Drude model[56] and Mermin model[57]. In these two models, the sum of the Drude-type ELFs in (4) is used to fit the optical ELF because both the extended Drude model and Mermin model coincide at the optical limit[58], that is, the Drude-type ELFs:

$$\mathrm{Im}\left[\frac{-1}{\varepsilon_D(0,\omega)}\right] = \mathrm{Im}\left[\frac{-1}{\varepsilon_M(0,\omega)}\right] = \sum_{i=1}^{n} A_i \frac{\gamma_i \omega}{\left(\omega^2 - \omega_{p,i}^2\right)^2 + \gamma_i^2 \omega^2}, \tag{9}$$

where $A_i = a_i \omega_{p,i}^2$ is the oscillator intensity, γ_i is the damping constant, and $\omega_{p,i}$ is the plasma

frequency.

The fitting model was built based on several previous studies[39, 40, 59, 60]. In the development of Geant4 MircoElec, Valentin[60] and Gibaru[40] *et al.* used a Heaviside step function to cut each oscillator in the fitting. Pablo *et al.*[61] used an exponential smooth switching function instead of a simple step function for the outer-shell electrons. Based on these prior methodologies, the fitting model is expressed as follows:

$$\text{Im}\left[\frac{-1}{\varepsilon(0,\omega)}\right] = \sum_{i=1}^{n} F(\omega)A_i \frac{\gamma_i\omega}{\left(\omega^2 - \omega_{p,i}^2\right)^2 + \gamma_i^2\omega^2}. \tag{10}$$

For the outer-shell electrons, $F(\omega)$ represents a smooth exponential switching function for the electronic excitations[61]:

$$F(\omega) = \frac{1}{1 + e^{-\Delta_i(\omega - \omega_{th.i})}}, \tag{11}$$

where Δ_i and $\omega_{th.i}$ are the additional fitting parameters. For the inner shells, particularly the K and L shells, which have sharp edges in the optical ELF, $F(\omega)$ is chosen as a simple step function $\Theta(\omega - \omega_{th,i})$. For plasmons and conduction band electrons, $F(\omega)$ can be simply set to 1.
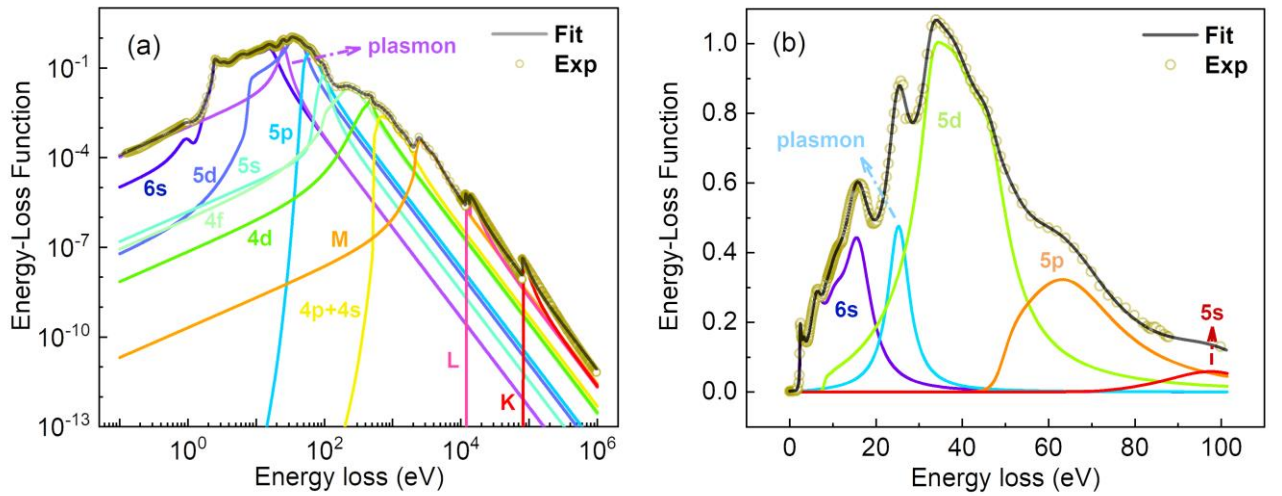
Fig. 2 Comparison of the fitted ELF (solid) and experimental ELF (circles): **a** contribution of each electronic shell obtained from the combined oscillators at the energy loss range of 0–100 eV; **b** contribution to all electronic shells of the combined oscillators

The experimental optical ELF, which covers the electron energies from 0.005 eV to 1 MeV, is derived from the databases of Palik[62], Windt[63], and the evaluated photo data library 1997 version (EPDL97[64]), in which the high-energy optical ELF is calculated using the photo-ionization cross

section[65] as follows:

$$\text{Im}\left[\frac{-1}{\varepsilon(0,\omega)}\right] = \frac{n_m c \sigma_{phot}}{\omega}, \tag{12}$$

where n_m is the atomic density, c is the speed of light, and σ_{phot} is the photoionization cross section.

The fitting results were validated by using two sum rules (*f*-sum and *ps*-sum) and the mean ionization potential. A partial *f*-sum rule for the fitted oscillators was also used to distinguish the contribution of the oscillators to the electronic shells. Initial values of the fitting (energy loss from 0 to 100 eV) were partially obtained by referring to the study of Pablo *et al*.[61]. We managed to use 28 oscillators to describe the optical ELF. **Fig. 2** demonstrates that the fitted ELF data sufficiently agrees with the experimental ELF.

During fitting, the plasmon peak was chosen as 25.42 eV, which is near 24.8 eV in Egerton's book[66]. We verified the *f*-sum rule of the fitted ELF, that is, $Z_{eff} = 78.05$ (ideal value: 79.0), while the *ps*-sum rule resulted in 1.0908 (ideal value: 1.0). The mean ionization potential based on the fitted ELF was 736.45 eV. These values obtained from the fitted ELF coincide with those from the experimental ELF, with only a small deviation in the high-energy region (L and K shells). This is likely due to the restriction of the Drude functions. If a more accurate experimental ELF is available, then better fitting results can be obtained. We also checked the partial *f*-sum rule to determine the shell to which the fitted oscillators belong, and the results are also displayed in **Fig. 2**. Therefore, these categorized oscillators enabled the calculation of the inelastic mean free path (IMFP) of the different shells.

The calculation of IMFP is achieved by extrapolating the momentum loss q from the optical limit to $q > 0$. For the extended Drude model, the extrapolation of q was achieved by using the dispersion relation. The extrapolation was performed using the following equation:

$$\text{Im}\left[\frac{-1}{\varepsilon_D(q,\omega)}\right] = \sum_{i=1}^{n} A_i \frac{\gamma_i(q)\omega}{\left(\omega^2 - \omega_{p,i}^2(q)\right)^2 + \gamma_i^2(q)\omega^2}. \tag{13}$$

In this method, $\omega_{p,i}(q)$ describes the plasmon dispersion and $\gamma_i(q)$ is the q-dependent damping constant, which represents the broadening effect. The variable γ_i is usually considered a constant; thus, one can simply choose (1) $\omega_{p,i}(q) = \omega_{p,i} + \frac{q^2}{2}$ or (2) $\omega_{p,i}(q) = \sqrt{\omega_{p,i}^2 + \frac{6E_F}{5}q^2 + \frac{q^2}{4}}$ [56, 67]. If γ_i is considered a function of q, another dispersion relation is given by[68, 69] (3) $\omega_{p,i}(q) =$

$\sqrt{\omega_{p,i}^2 + \frac{2E_F}{3}q^2 + \frac{q^2}{4}}$ and $\gamma_i(q) = \sqrt{\gamma_i^2 + \frac{q^2}{4}}$. This was already presented in the study of Ritchie *et al.*[56] and proved[68] to be more comprehensive than the extrapolation considering only the $\omega_{p,i}(q)$. Therefore, we chose the third extrapolation method for the conduction band and outer shells and the first method for the inner shells as the first inelastic model, which is labeled as Ritchie in the following text.

Regarding the Mermin model, the extrapolation procedure was already achieved using the Mermin dielectric function[70] as follows:

$$\varepsilon_M(q, \omega) = 1 + \frac{\left(1 + \frac{i\gamma}{\omega}\right)[\varepsilon_L(q, \omega + i\gamma) - 1]}{1 + \frac{i\gamma}{\omega}[\varepsilon_L(q, \omega + i\gamma) - 1]/(\varepsilon_L(q, 0) - 1)}, \tag{14}$$

where ε_L is the Lindhard dielectric function[71] and $\varepsilon_L(q, 0)$ is the Lindhard dielectric function at the static limit. This is the second inelastic model, which is also labeled as Mermin.

A significant advantage of the extended Drude model and Mermin model is that fitted oscillators can approximate the contribution to particular electronic shells or the plasmon in the calculation. Therefore, combined with the divided shells in the ELF, we can calculate the IMFP of the different electronic shells.

The general calculation of IMFP considering the relativistic high energy correction is performed by

$$\lambda_{inel}^{-1}(E) = \frac{\left(1 + \frac{E}{c^2}\right)^2}{1 + \frac{E}{2c^2}} \frac{1}{\pi E} \int_{W_-}^{W_+} d\omega \int_{q_-}^{q_+} f_{ex}(q, E) \frac{dq}{q} F(\omega) \text{Im}\left[\frac{-1}{\varepsilon(q, \omega)}\right], \tag{15}$$

where E is the kinetic energy of the incident electrons, c is the speed of light, $\frac{\left(1 + \frac{E}{c^2}\right)^2}{1 + \frac{E}{2c^2}}$ is the relativistic correction, W_+ is the maximum energy loss, W_- is the minimum energy loss, and q_+ and q_- are the maximum and minimum momentum losses, respectively. The variables q_+ and q_- are given by

$$q_\pm = \sqrt{E\left(2 + \frac{E}{c^2}\right) \pm \sqrt{(E - \omega)\left(2 + \frac{E - \omega}{c^2}\right)}}, \tag{16}$$

where $f_{ex}(q, E) = 1 - \frac{q^2}{2E} + \left(\frac{q^2}{2E}\right)^2$ is the Ochkur exchange correction[72]. For a collective excitation, $f_{ex} = 1$. As indicated above, $F(\omega)$ is an exponential switching function or a simple step function.

The inelastic cross sections of each shell were individually calculated. For metals such as Au, W_- equals zero. As proposed by Pablo *et al.*[61], the maximum energy loss W_+ depends on the different

electronic shells. Plasmon and 5d electrons are considered collective excitations; thus, $W_+ = E - E_F$. For the outer-shell and inner-shell electrons, W_+ equals $\min[E - E_F, (E + B_i)/2]$, where B_i is the binding energy of the i-th electronic shell. The binding energies of the outer- and inner-shell electrons were derived from the FFAST database[73]. Meanwhile, a classical Coulomb-field Born correction that accounts for the potential energy gained by the incident electrons is added for the calculation of the outer-shell and inner-shell electrons. This is achieved by replacing the kinetic energy E with $E' = E + 2B_i$ in the calculation; however, the energy loss should remain unchanged.

Based on the aforementioned discussion, we compared calculated IMFP with previously reported experimental[74-76] and theoretical data[77-86], which are shown in **Fig. 3**.
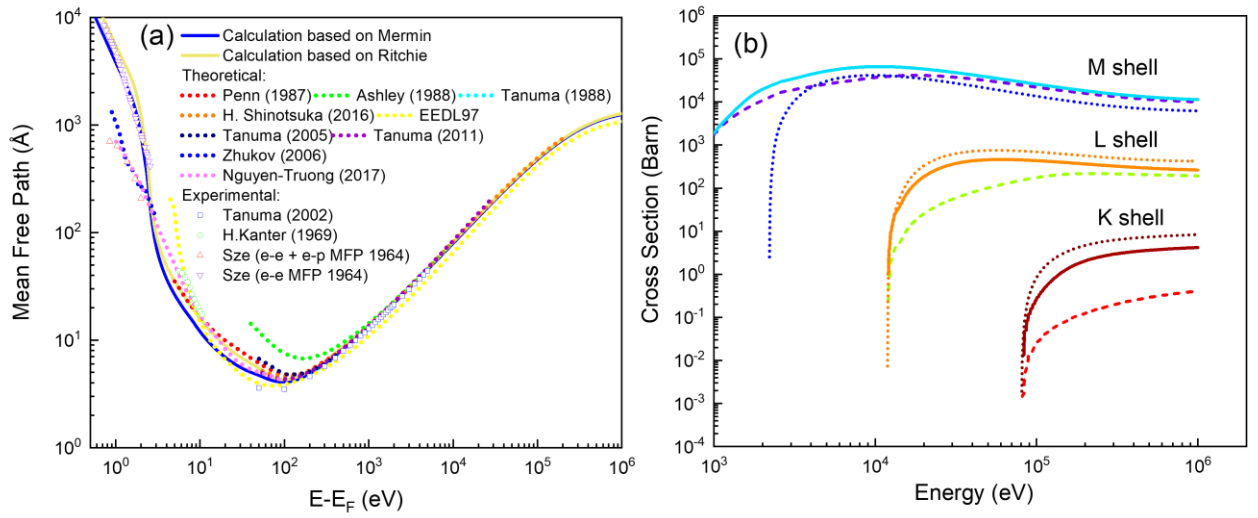
Fig. 3 a Calculated inelastic mean free path and comparison with other published data[74-76]. **b** Calculated inner shell cross sections (K, L, M shells); solid, dashed, and dotted lines indicate the Ritchie model, Mermin model, and Gryzinski theory, respectively[87, 88]

Fig. 3a presents the calculated IMFP, which sufficiently agrees with the experimental and previous theoretical data. A relativistic effect is clearly observed at high energies. At low energies below 100 eV, the modified Ritchie model can derive a good IMFP similar to that of the Mermin model due to its improved estimation of the plasmon lifetime by considering γ as a function of q. We also calculated the inner-shell ionization cross sections and compared them with the relativistic Gryzinski's formula[87, 88] for validation. As shown in **Fig.** 3b, the calculation using the Ritchie model can yield better inner-shell ionization data compared to the Mermin model, which indicates that the Ritchie model is recommended for high-energy electron simulations. This may be due to the fact that for the inner-shells, the plasmonic consideration in the Mermin model is no longer valid, whereas in the

Ritchie model, the simple extrapolation of q without considering the plasmon is more applicable. Although the inner shell cross sections using both the Ritchie and Mermin models remain lower than those calculated by the Gryzinski theory, which is considered more accurate, this may be due to the fact that the fitted ELF is insufficiently accurate for the inner shells. Therefore, this lowers the accuracy of the calculated inner-shell cross sections.

Following an inelastic event, in normal considerations, a secondary electron will be generated with an energy of $E_S = W + E_F$ for Fermi electron excitation (conduction band and plasmon excitation as considered in this study) and $E_S = W - B_i$ for the inner- and outer-shell ionization, where W is the energy loss. In this case, we applied the improvement made by Ding et al.[89], which assumes that the initial energy E' of the Fermi electron is proportional to the joint density of states (JDOS) of the free-electron gas, that is, $P(E', W) \propto \sqrt{E'(E' + W)}$. In the expression, E' must satisfy $E' < E_F$ and $E' + W > E_F$. Therefore, the modified energy of the Fermi electron after inelastic scattering is $E_S = W + E'$.

2.3 Surface Potential

For an electron to escape from the surface of metals, it must have a kinetic energy larger than the Fermi level E_F and the work function W_F, that is, the potential barrier between the metal surface and vacuum[89]. Therefore, the cut-off energy in the simulation is set to $E_F + W_F$, and the electrons are locally terminated below this limit, which can also save memory.

To escape from the surface, once an electron reaches the gold surface, its kinetic energy must satisfy the following condition:

$$E\cos^2\theta > U, \tag{17}$$

where E is the energy that considers the Fermi level as the zero point, θ is the angle between the electron motion direction and is normal to the surface before its emission, and $U = W_F$ is the potential barrier above the Fermi level. Subsequently, according to the quantum theory, the emission will depend on the transmission coefficient T[89-91], which is given by the following:

$$T = \frac{4\sqrt{1 - U/(E\cos^2\theta)}}{\left[1 + \sqrt{1 - U/(E\cos^2\theta)}\right]^2}. \tag{18}$$

A random number R is generated for comparison with T to determine the emission as follows:

$$\begin{cases} \text{Emission,} & \text{if } R < T \\ \text{Reflection,} & \text{else} \end{cases}. \tag{19}$$

The emitted electrons have a kinetic energy of $E - U$, and electrons entering the solid will also gain potential energy W_F above the Fermi level. In the SEE simulation, the work function between the gold surface and vacuum was set to 5.1 eV. Considering practical cases of water-gold interfaces for future development, we will use the difference between the work functions of these two materials and assume that the calculation of the transmission coefficient is similar to that considered in the surface-vacuum interface.

3 Results and Discussion:

3.1 Secondary electron emission

3.1.1 Secondary electron yield

To validate the code, we simulated SEE experiments and calculated the secondary electron yield (SEY) and backscattering coefficient (BSC) of gold. This simulation was simply set up as multiple groups of mono-energetic electron beams vertically bombarding an infinite gold plane, and the information of the electrons emitted from the surface was collected. The SEY is defined as the ratio of the number of emitted secondary electrons (< 50 eV) to the number of incident primary electrons. The BSC is defined as the ratio of the number of backscattering electrons (> 50 eV) to the number of incident primary electrons. To obtain the SEY and BSC, 1×10^6 particles were simulated. The uncertainty of this code in the SEE simulation is less than 1%. As presented in **Fig. 4**, we demonstrate the calculated SEY and BSC and compare them with the experimental data collected by Joy *et al.*[92]. Regarding the experimental data, monoenergetic electron beams were used in most of the experiments to bombard the material under vacuum conditions, which was similar to the simulation setup.
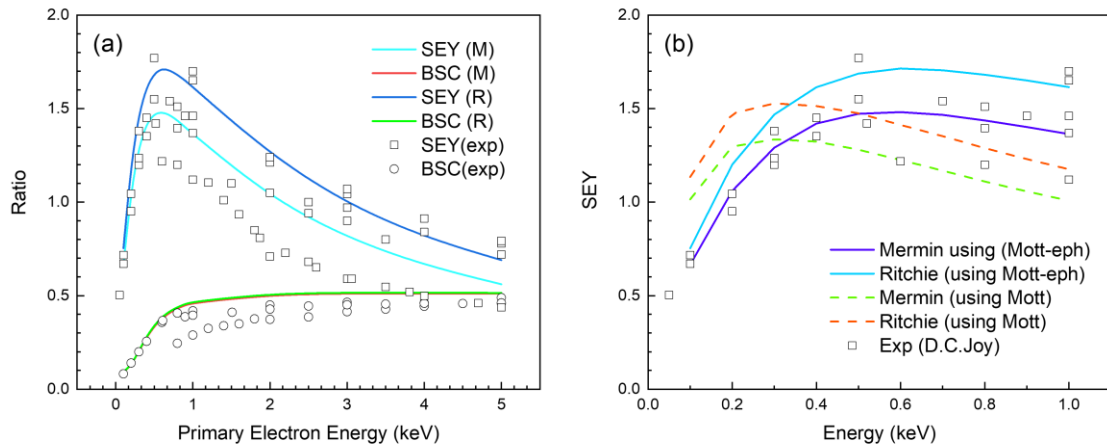
Fig. 4 a SEY and BSC derived from the SEE simulations and compared to the experimental data[92]; M indicates the Mermin model and R indicates the Ritchie model. **b** Comparison of the SEY values calculated by two ways (solid lines: Mott-eph, dashed lines: Mott)

As shown in **Fig.** 4a, the simulated SEY values mostly coincide with the experimental values[92], which is essential for the calculation of the emission of LEEs from AuNPs. The Ritchie model derived a larger SEY compared to the Mermin model, whereas the BSC values were similar in both models. In addition, if the modification for low-energy elastic scattering was not added, the SEY values calculated in both ways would mainly differ below 1 keV, as shown in **Fig.** 4b. The figure shows that the calculated SEY using only the Mott cross sections is larger than the experimental values for the primary electrons with a lower energy (< 400 eV). The modification of the elastic cross sections improved the description of the SEE. The high SEY also suggests that the ^{125}I emitted electrons can enhance the LEE emission from gold nanoparticles.

3.1.2 Secondary electron spectra

The secondary electron spectra are critical for the analysis of LEEs emitted from AuNPs because the cross sections of the LEEs damaging the DNA, such as DSBs and SSBs, are highly energy-dependent[9]. The 1×10^7 electrons were simulated to obtain stable secondary electron spectra, which are presented in **Fig. 5**. The figure demonstrates that most of the emitted secondary electrons were below 30 eV; a zero-loss elastic peak is also observed herein.
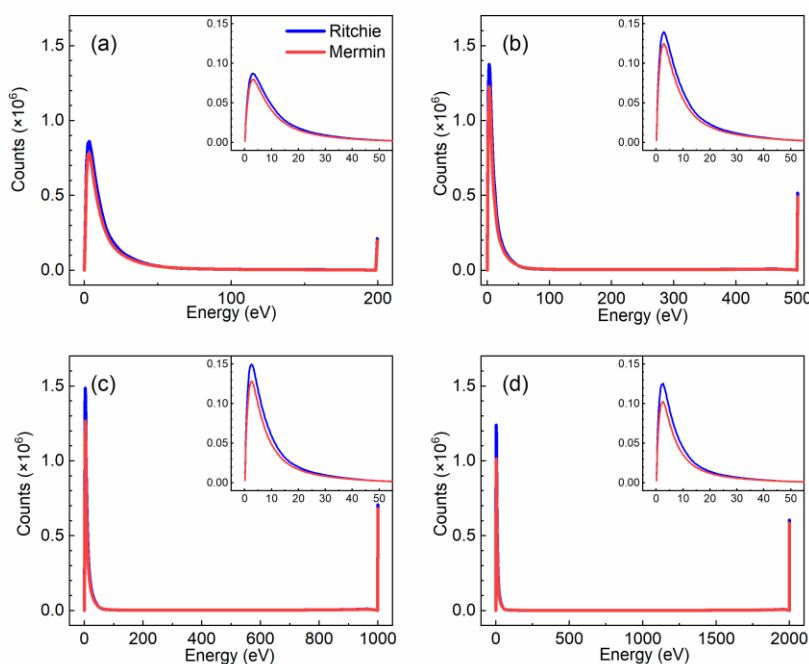
Fig. 5 Emitted electron spectra from SEE simulations: **a** 200 eV primary electrons, **b** 500 eV primary electrons, **c** 1 keV primary electrons, and **d** 2 keV primary electrons

Moreover, the peak of LEEs was found to be located at 2.25–3.25 eV, which is similar to the 2.2 eV peak value reported in the ion-bombardment SEE experiment[93]. This large amount of LEE emission also suggests the feasibility of using sub-keV electrons combined with AuNPs as a high-flux LEE source.

3.2 Dosimetry test

Dosimetry testing is critical for the evaluation of further microdosimetry. The stopping power, $S(E)$, for electrons of energy E can be calculated using a method similar to the IMFP. The expression for $S(E)$ is shown below:

$$S(E) = \frac{\left(1 + \frac{E}{c^2}\right)^2}{1 + \frac{E}{2c^2}} \frac{1}{\pi E} \int_{W_-}^{W_+} \omega d\omega \int_{q_-}^{q_+} f_{ex}(q, E) \frac{dq}{q} F(\omega) \text{Im} \left[\frac{-1}{\varepsilon(q, \omega)}\right]. \tag{20}$$

As shown in **Fig. 6**, we compared the calculated stopping power with those of other theoretical calculations[81, 85, 94-97] and experiments[98]. The effect of the relativistic corrections introduced in the calculation is demonstrated by the stopping powers at high electron energies, which is in good agreement with the ESTAR[85] and the evaluated electron data library (EEDL) databases[81]. With the modifications, the Ritchie model can produce an accurate stopping power comparable to that of the Mermin model at low energies.
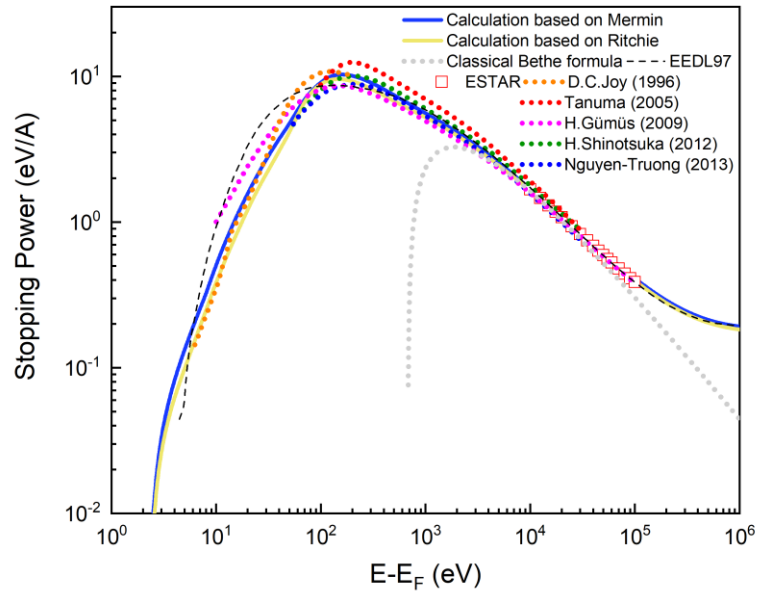
Fig. 6 Calculated stopping power and comparison with other published data[81, 85, 94-97]

The energy deposition was mainly tested using the semi-infinite gold model. Calculation of the energy deposition depth profiles can provide information regarding the energy deposited in gold and its uniformity. This verification also guarantees the correctness of dosimetry for future studies. Electron energy deposition as a function of the depth of semi-infinite gold was calculated for comparison using the developed code and Geant4 standard electromagnetic physics (option 4). In the calculation, 200 eV, 500 eV, 1 keV, 2 keV, and 10 keV electrons were simulated; 5×10^6 electrons were adopted in each test. The calculated results are shown in **Fig. 7**.
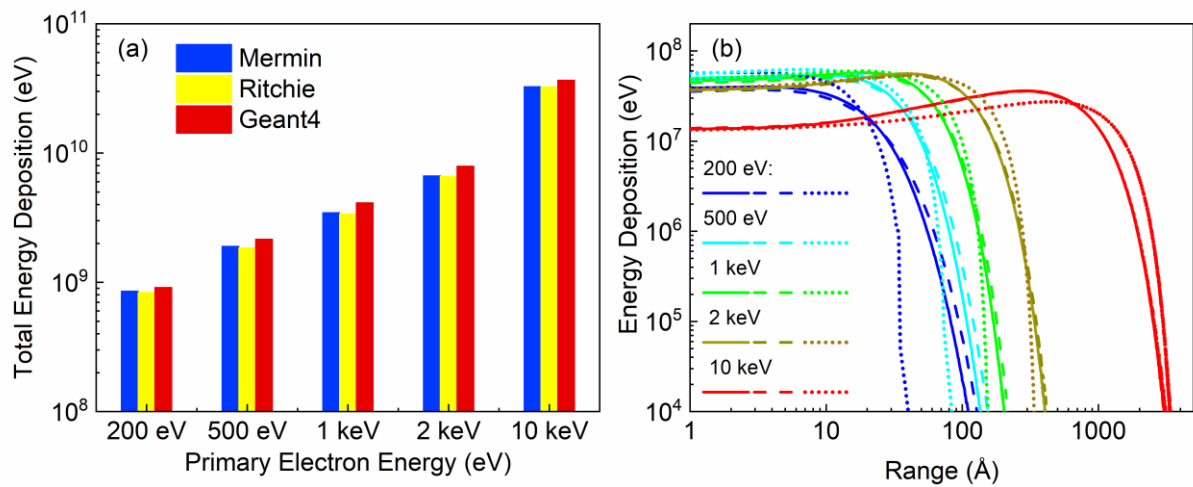
Fig. 7 a Calculated total energy deposition. **b** Calculated energy deposition as a function of depth (1 – 1000 Å with 1 Å as the thickness of each layer) using the developed code (solid and dashed lines indicate the Mermin and Ritchie models, respectively) and Geant4 (dotted line)

The outcomes of both inelastic models in the code present a similar tendency. **Fig. 7 (a)** demonstrates that the ratio of the total energy deposition results of this code to that of Geant4 was approximately 89%–93%. This slight decrease was due to the larger secondary electron emission from the surface. In contrast, the difference in the energy deposition depth profiles is shown in **Fig. 7 (b).** At low energies, our inelastic cross sections differ from those of the Livermore model (EEDL[81]). Gibaru *et al.*[40] suggested that the Geant4 standard physics underestimates the range of electrons, which is also observed upon comparing our results. At high energies, the energy deposition depth profiles of both this code and Geant4 tended to coincide. Note that the more detailed energy-straggling strategy in this code is significantly slower than the multiple scattering strategy in Geant4 standard physics.

A function for calculating the energy deposition in the 3D voxels was also added to enable future microdosimetry studies. The method for calculating the energy deposition in the 3D voxels is demonstrated, and the calculation is displayed in **Fig. 8**. The length of the 3D voxels was set to 1 Å, and the maximum length of each axis was 1000 Å. The 1×10^7 electrons were simulated here.
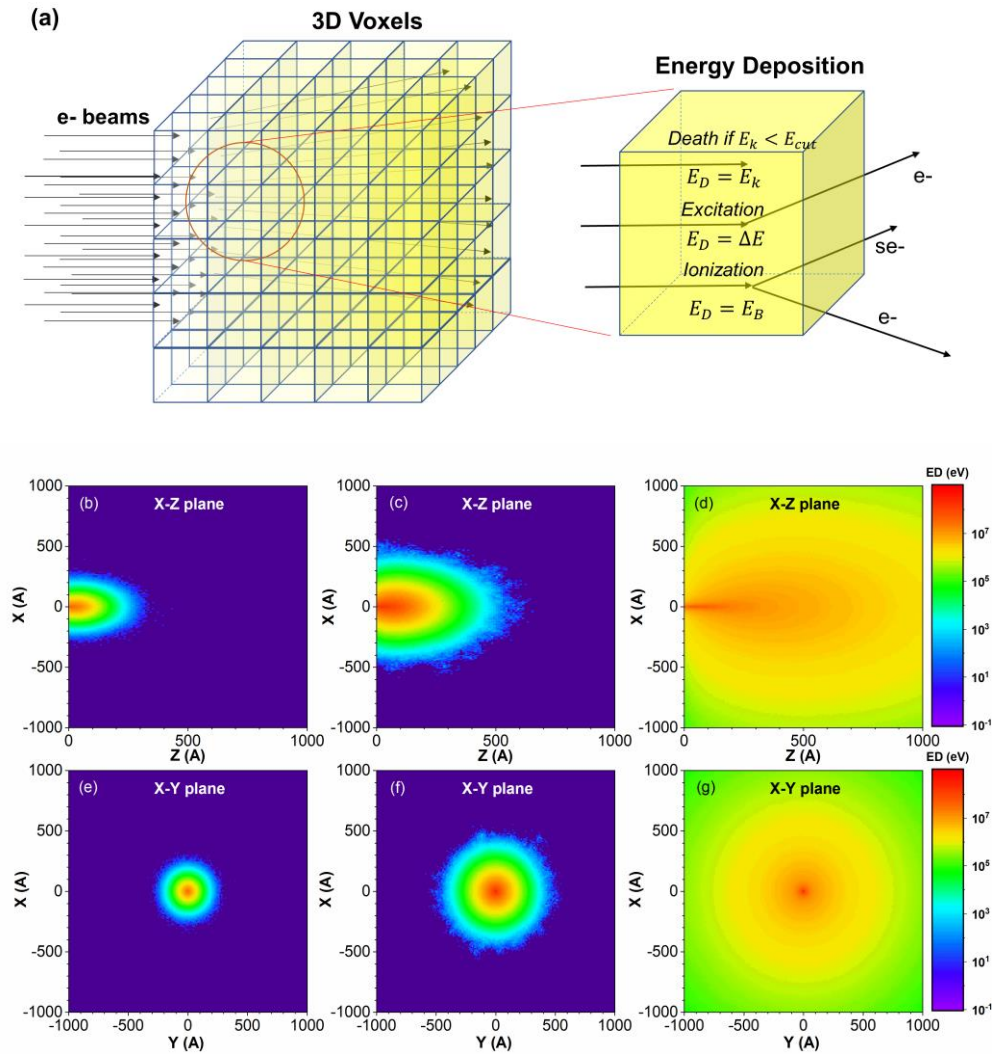
Fig. 8 a Diagram of the calculation of the energy deposition in 3d voxels; projection of the calculated energy deposition (Ritchie) by the 3D voxels. **b** 1 keV X-Z plane, **c** 2 keV X-Z plane, **d** 10 keV X-Z plane, **e** 1 keV X-Y plane, **f** 2 keV X-Y plane, and **g** 10 keV X-Y plane

In **Fig. 8**, the spatial distribution of the energy deposition demonstrates good symmetry, which verifies the particle transport in the Monte Carlo procedure. The intensity of the energy deposition in the X-Z plane is more comprehensive than that of the depth profiles. At low energies, the projection of energy deposition in the X-Z plane is an ellipse around the entry point of the electron beams. As the incident electron energy increases, the energy deposition distribution tends to become more

cylindrical. The distribution of the energy deposition also demonstrates the nanoscale precision of this code. This function allowed the further visualization and analysis of the electron energy deposition inside the AuNPs when irradiated with electrons.

4 Conclusion

A Monte Carlo code was built to simulate the nanoscale electron transport in gold material down to 0.5 eV above the Fermi level. Mott elastic scattering cross sections were calculated using the ELSEPA code[44]. Electron-acoustic phonon cross sections were calculated from the fitted dispersion relation. The elastic cross sections were modified using a truncation method that applies Mott cross sections at energies higher than 100 eV, electron-phonon cross sections at 0–50 eV, and interpolation in between. The optical ELF data were fitted into 28 Drude oscillators, which were categorized into different electronic shells to calculate the cross sections using the dielectric theory. Two inelastic models, the Ritchie and Mermin models, were used to produce inelastic cross sections. The exchange effect, Born correction, and relativistic effects were carefully considered. The initial energy of the Fermi electrons in the conduction band electron excitation was refined from the Fermi energy to the sampled energy from the JDOS.

We simulated and compared the SEE results with the experimental results and found a reasonable agreement. The quantum model of the surface potential plays an important role in the calculation of the SEE from the surface. The simulated secondary electron spectra demonstrate a high yield of LEEs from the gold surface when irradiated with keV electrons. Thus, building such a simulation code is significant for studying LEEs in micro- and nanodosimetry. The inelastic stopping power and energy deposition depth profiles were validated. The 3D voxel function was implemented in the developed code to allow further usage.

This code is planned for the evaluation of the LEE emission in the ^{125}I/AuNPs system. It is also being developed for its significant potential in future microdosimetry studies. Further improvements in this code include considering the structure of small AuNPs, implementing the surface plasmon mode for certain AuNPs, adding more materials, and using an advanced geometry intersection algorithm.

first draft of the manuscript was written by Liheng Zhou and all authors commented on previous versions of the manuscript. All authors read and approved the final manuscript.

References

1. J. G. Kereiakes, D. V. Rao, Auger electron dosimetry: report of AAPM Nuclear Medicine Committee Task Group No. 6. Med. Phys.**, 19** (6), 1359 (1992). https://doi.org/10.1118/1.596925

2. A. I. Kassis, Therapeutic radionuclides: biophysical and radiobiologic principles. Semin. Nucl. Med.**, 38** (5), 358-66 (2008). https://doi.org/10.1053/j.semnuclmed.2008.05.002

3. I. Kyriakou, I. Tremi, A. G. Georgakilas, et al., Microdosimetric investigation of the radiation quality of low-medium energy electrons using Geant4-DNA. Appl. Radiat. Isot.**, 172**, 109654 (2021). https://doi.org/10.1016/j.apradiso.2021.109654

4. J. A. O'Donoghue, T. E. Wheldon, Targeted radiotherapy using Auger electron emitters. Phys. Med. Biol.**, 41** (10), 1973-92 (1996). https://doi.org/10.1088/0031-9155/41/10/009

5. A. Mozumder, Ionization and excitation yields in liquid water due to the primary irradiation: Relationship of radiolysis with far UV-photolysisPresented at the Symposium on Recent Trends in Photochemical Sciences, Trivandrum, January 8-10, 2000. Phys. Chem. Chem. Phys.**, 4** (8), 1451-1456 (2002). https://doi.org/10.1039/b106017c

6. L. Sanche, Low energy electron-driven damage in biomolecules. Eur. Phys. J. D**, 35** (2), 367-390 (2005). https://doi.org/10.1140/epjd/e2005-00206-6

7. B. Boudaiffa, P. Cloutier, D. Hunting, et al., Resonant formation of DNA strand breaks by low-energy (3 to 20 eV) electrons. Science**, 287** (5458), 1658-1660 (2000). https://doi.org/10.1126/science.287.5458.1658

8. R. Barrios, P. Skurski, J. Simons, Mechanism for damage to DNA by low-energy electrons. J. Phys. Chem. B**, 106** (33), 7991-7994 (2002). https://doi.org/10.1021/jp013861i

9. W. Chen, S. Chen, Y. Dong, et al., Absolute cross-sections for DNA strand breaks and crosslinks induced by low energy electrons. Phys. Chem. Chem. Phys.**, 18** (48), 32762-32771 (2016). https://doi.org/10.1039/c6cp05201k

10. *Nanoparticle Enhanced Radiation Therapy*. (IOP Publishing: 2020)

11. P.-Y. Qi, Z.-T. Dai, J. Zhang, et al., Investigation of the radiosensitization effect in FePt nanopaticle clusters with Monte Carlo simulation. Nucl. Sci. Tech.**, 29** (11), 167 (2018). https://doi.org/10.1007/s41365-018-0495-9

12. M. Y. Chang, A. L. Shiau, Y. H. Chen, et al., Increased apoptotic potential and dose-enhancing effect of gold nanoparticles in combination with single-dose clinical electron beams on tumor-bearing mice. Cancer Sci.**, 99** (7), 1479-1484 (2008). https://doi.org/10.1111/j.1349-

7006.2008.00827.x

13. J. F. Hainfeld, D. N. Slatkin, H. M. Smilowitz, The use of gold nanoparticles to enhance radiotherapy in mice. **49** (18), N309-N315 (2004). https://doi.org/10.1088/0031-9155/49/18/n03

14. H. Nikjoo, L. Lindborg, RBE of low energy electrons and photons. Phys. Med. Biol.**, 55** (10), R65-109 (2010). https://doi.org/10.1088/0031-9155/55/10/R01

15. S. M. Pimblott, J. A. LaVerne, A. Mozumder, Monte Carlo simulation of range and energy deposition by electrons in gaseous and liquid water. J. Phys. Chem.**, 100** (20), 8595-8606 (1996). https://doi.org/10.1021/jp9536559

16. L. Sanche, Cancer treatment: Low-energy electron therapy. Nat. Mater.**, 14** (9), 861-863 (2015). https://doi.org/10.1038/nmat4333

17. E. Alizadeh, L. Sanche, Precursors of solvated electrons in radiobiological physics and chemistry. Chem. Rev.**, 112** (11), 5578-5602 (2012). https://doi.org/10.1021/cr300063r

18. J. Meesungnoen, J.-P. Jay-Gerin, A. Filali-Mouhim, et al., Low-energy electron penetration range in liquid water. Radiat. Res.**, 158** (5), 657-660 (2002). https://doi.org/10.1667/0033-7587(2002)158[0657:Leepri]2.0.Co;2

19. A. Pronschinske, P. Pedevilla, C. J. Murphy, et al., Enhancement of low-energy electron emission in 2D radioactive films. Nat. Mater.**, 14** (9), 904-7 (2015). https://doi.org/10.1038/nmat4323

20. A. Ku, V. J. Facca, Z. Cai, et al., Auger electrons for cancer therapy - a review. EJNMMI Radiopharm. Chem.**, 4** (1), 27 (2019). https://doi.org/10.1186/s41181-019-0075-2

21. H. Seiler, Secondary electron emission in the scanning electron microscope. J. Appl. Phys.**, 54** (11), R1-R18 (1983). https://doi.org/10.1063/1.332840

22. Y. Lin, D. C. Joy, A new examination of secondary electron yield data. Surf. Interface Anal.**, 37** (11), 895-900 (2005). https://doi.org/10.1002/sia.2107

23. L. A. Gonzalez, M. Angelucci, R. Larciprete, et al., The secondary electron yield of noble metal surfaces. AIP Adv.**, 7** (11), 115203 (2017). https://doi.org/10.1063/1.5000118

24. M. Dapor, *Transport of Energetic Electrons in Solids. Computer Simulation with Applications to Materials Analysis and Characteriza-tion*. 3 ed. (Springer International Publishing AG, Cham: 2020)

25. D. Emfietzoglou, G. Papamichael, K. Kostarelos, et al., A Monte Carlo track structure code for electrons (~10 eV–10 keV) and protons (~0.3–10 MeV) in water: partitioning of energy and collision events. Phys. Med. Biol.**, 45** (11), 3171-3194 (2000). https://doi.org/10.1088/0031-9155/45/11/305

26. S. Agostinelli, J. Allison, K. Amako, et al., Geant4—a simulation toolkit. Nucl. Instrum. Methods. Phys. Res. B**, 506** (3), 250-303 (2003). https://doi.org/10.1016/s0168-9002(03)01368-8

27. R. A. Forster, L. J. Cox, R. F. Barrett, et al., MCNP™ version 5. **213**, 82-86 (2004). https://doi.org/10.1016/s0168-583x(03)01538-6

28. L. Deng, G. Li, B.-Y. Zhang, et al., A high fidelity general purpose 3-D Monte Carlo particle transport program JMCT3.0. Nucl. Sci. Tech.**, 33** (8), 108 (2022). https://doi.org/10.1007/s41365-022-01092-0

29. Y. Wu, J. Song, H. Zheng, et al., CAD-based Monte Carlo program for integrated simulation of nuclear system SuperMC. Ann. Nucl. Energy**, 82**, 161-168 (2015). https://doi.org/10.1016/j.anucene.2014.08.058

30. I. Kawrakow, Accurate condensed history Monte Carlo simulation of electron transport. I. EGSnrc, the new EGS4 version. **27** (3), 485-498 (2000). https://doi.org/10.1118/1.598917

31. S. Incerti, G. Baldacchino, M. Bernal, et al., The Geant4-DNA Project. Int. J. Model. Simul. Sci. Comput.**, 01** (02), 157-178 (2012). https://doi.org/10.1142/S1793962310000122

32. M. A. Bernal, M. C. Bordage, J. M. C. Brown, et al., Track structure modeling in liquid water: A review of the Geant4-DNA very low energy extension of the Geant4 Monte Carlo simulation toolkit. Phys. Med., **31** (8), 861-874 (2015). https://doi.org/10.1016/j.ejmp.2015.10.087

33. S. Incerti, A. Ivanchenko, M. Karamitros, et al., Comparison of GEANT4 very low energy cross section models with experimental data in water. Med. Phys., **37** (9), 4692-4708 (2010). https://doi.org/10.1118/1.3476457

34. S. Incerti, I. Kyriakou, M. A. Bernal, et al., Geant4-DNA example applications for track structure simulations in liquid water: A report from the Geant4-DNA Project. Med. Phys., **45** (8), e722-e739 (2018). https://doi.org/10.1002/mp.13048

35. V. A. Semenenko, J. E. Turner, T. B. Borak, NOREC, a Monte Carlo code for simulating electron tracks in liquid water. Radiat. Environ. Biophys., **42** (3), 213-217 (2003). https://doi.org/10.1007/s00411-003-0201-z

36. T. Liamsuwan, D. Emfietzoglou, S. Uehara, et al., Microdosimetry of low-energy electrons. Int. J. Radiat. Biol., **88** (12), 899-907 (2012). https://doi.org/10.3109/09553002.2012.699136

37. D. Alloni, A. Campa, W. Friedland, et al., Track structure, radiation quality and initial radiobiological events: considerations based on the PARTRAC code experience. Int. J. Radiat. Biol., **88** (1-2), 77-86 (2012). https://doi.org/10.3109/09553002.2011.627976

38. D. Sakata, S. Incerti, M. C. Bordage, et al., An implementation of discrete electron transport models for gold in the Geant4 simulation toolkit. J. Appl. Phys., **120** (24), 244901 (2016). https://doi.org/10.1063/1.4972191

39. D. Sakata, I. Kyriakou, H. N. Tran, et al., Electron track structure simulations in a gold nanoparticle using Geant4-DNA. Phys. Med., **63**, 98-104 (2019). https://doi.org/10.1016/j.ejmp.2019.05.023

40. Q. Gibaru, C. Inguimbert, P. Caron, et al., Geant4 physics processes for microdosimetry and secondary electron emission simulation: extension of MicroElec to very low energies and 11 materials (C, Al, Si, Ti, Ni, Cu, Ge, Ag, W, Kapton and SiO_2). Nucl. Instrum. Methods Phys. Res. B, **487**, 66-77 (2021). https://doi.org/10.1016/j.nimb.2020.11.016

41. T.-L. He, H.-L. Xu, K.-T. Huang, et al., Monte Carlo simulation of incident electrons passing through thin metal layer. Nucl. Sci. Tech., **29** (7), 103 (2018). https://doi.org/10.1007/s41365-018-0429-6

42. M.-T. Tang, L.-J. Mao, H.-J. Lu, et al., Design of an efficient collector for the HIAF electron cooling system. Nucl. Sci. Tech., **32** (10), 116 (2021). https://doi.org/10.1007/s41365-021-00949-0

43. N. F. Mott, N. H. D. Bohr, The scattering of fast electrons by atomic nuclei. Proc. Math. Phys. Eng. Sci., **124** (794), 425-442 (1929). https://doi.org/10.1098/rspa.1929.0127

44. F. Salvat, A. Jablonski, C. J. Powell, elsepa—Dirac partial-wave calculation of elastic scattering of electrons and positrons by atoms, positive ions and molecules. Comput. Phys. Commun., **165** (2), 157-190 (2005). https://doi.org/10.1016/j.cpc.2004.09.006

45. F. Salvat, A. Jablonski, C. J. Powell, elsepa—Dirac partial-wave calculation of elastic scattering of electrons and positrons by atoms, positive ions and molecules (New Version Announcement). Comput. Phys. Commun., **261**, 107704 (2021). https://doi.org/10.1016/j.cpc.2020.107704

46. J. W. Lynn, H. G. Smith, R. M. Nicklow, Lattice dynamics of gold. Phys. Rev. B, **8** (8), 3493-3499 (1973). https://doi.org/10.1103/PhysRevB.8.3493

47. E. Schreiber, H. J. Fitting, Monte Carlo simulation of secondary electron emission from the insulator SiO_2. J. Electron. Spectrosc. Relat. Phenom., **124** (1), 25-37 (2002). https://doi.org/10.1016/s0368-2048(01)00368-1

48. H. J. Fitting, E. Schreiber, J. C. Kuhr, et al., Attenuation and escape depths of low-energy electron emission. J. Electron. Spectrosc. Relat. Phenom., **119** (1), 35-47 (2001). https://doi.org/10.1016/s0368-2048(01)00232-8

49. T. Verduin. *Quantum noise effects in e beam lithography and metrology*. (Delft University of Technology, 2017)

50. A. M. M. G. Theulings. *Optimisation of photon detector tynode membranes using electron matter scattering simulations*. (Faculty of Applied Sciences, Delft University of Technology, Department of Imaging Physics, 2020)

51. J. N. Bradford, S. Woolf, Electron-acoustic phonon scattering in SiO_2 determined from a pseudo-potential for energies of $E > E_{BZ}$. J. Appl. Phys., **70** (1), 490-492 (1991). https://doi.org/10.1063/1.350254

52. E. Kieft, E. Bosch, Refinement of Monte Carlo simulations of electron–specimen interaction in low-voltage SEM. J. Phys. D, **41** (21), 215310 (2008). https://doi.org/10.1088/0022-3727/41/21/215310

53. R. H. Ritchie, Plasma Losses by Fast Electrons in Thin Films. Phys. Rev., **106** (5), 874-881 (1957). https://doi.org/10.1103/PhysRev.106.874

54. M. Vos, P. L. Grande, Extracting the dielectric function from high-energy REELS measurements. Surf. Interface Anal., **49** (9), 809-821 (2017). https://doi.org/10.1002/sia.6227

55. W. S. M. Werner, K. Glantschnig, C. Ambrosch-Draxl, Optical constants and inelastic electron-scattering data for 17 elemental metals. J. Phys. Chem. Ref. Data, **38** (4), 1013-1092 (2009). https://doi.org/10.1063/1.3243762

56. R. H. Ritchie, A. Howie, Electron excitation and the optical potential in electron microscopy. The Philosophical Magazine: A Journal of Theoretical Experimental and Applied Physics, **36** (2), 463-481 (1977). https://doi.org/10.1080/14786437708244948

57. I. Abril, R. Garcia-Molina, C. D. Denton, et al., Dielectric description of wakes and stopping powers in solids. Phys. Rev. A, **58** (1), 357-366 (1998). https://doi.org/10.1103/PhysRevA.58.357

58. M. Vos, A model dielectric function for low and very high momentum transfer. Nucl. Instrum. Methods Phys. Res. B, **366**, 6-12 (2016). https://doi.org/10.1016/j.nimb.2015.09.091

59. Y. Sun, H. Xu, B. Da, et al., Calculations of energy-loss function for 26 materials. Chinese J. Chem. Phys., **29** (6), 663-670 (2016). https://doi.org/10.1063/1674-0068/29/cjcp1605110

60. A. Valentin, M. Raine, J. E. Sauvestre, et al., Geant4 physics processes for microdosimetry simulation: very low energy electromagnetic models for electrons in silicon. Nucl. Instrum. Methods Phys. Res. B, **288**, 66-73 (2012). https://doi.org/10.1016/j.nimb.2012.07.028

61. P. de Vera, R. Garcia-Molina, Electron inelastic mean free paths in condensed matter down to a few electronvolts. J. Phys. Chem. C, **123** (4), 2075-2083 (2019). https://doi.org/10.1021/acs.jpcc.8b10832

62. E. D. Palik, *Handbook Optical Constants of Solids* 3rd ed. (Academic Press: 1998)

63. D. L. Windt, W. C. Cash, Jr., M. Scott, et al., Optical constants for thin films of Ti, Zr, Nb, Mo, Ru, Rh, Pd, Ag, Hf, Ta, W, Re, Ir, Os, Pt, and Au from 24 A to 1216 A. Appl. Opt., **27** (2), 246-278 (1988). https://doi.org/10.1364/ao.27.000246

64. D. E. Cullen, J. H. Hubbell, L. Kissel *EPDL97: the evaluated photo data library `97 version*; United States, 1997.

65. U. Fano, J. W. Cooper, Spectral distribution of atomic oscillator strengths. Rev. Mod. Phys., **40** (3), 441-507 (1968). https://doi.org/10.1103/RevModPhys.40.441

66. R. F. Egerton, *Electron Energy-Loss Spectroscopy in the Electron Microscope*. (Springer New York: New York, 2011)

67. D. Emfietzoglou, I. Kyriakou, R. Garcia-Molina, et al., The effect of static many-body local-field corrections to inelastic electron scattering in condensed media. J. Appl. Phys., **114** (14), 144907 (2013). https://doi.org/10.1063/1.4824541

68. L. H. Yang, K. Tőkési, J. Tóth, et al., Optical properties of silicon and germanium determined by high-precision analysis of reflection electron energy loss spectroscopy spectra. Phys. Rev. B**, 100** (24), 245209 (2019). https://doi.org/10.1103/PhysRevB.100.245209

69. R. A. Ferrell, Characteristic energy loss of electrons passing through metal foils. II. Dispersion relation and short wavelength cutoff for plasma oscillations. Phys. Rev.**, 107** (2), 450-462 (1957). https://doi.org/10.1103/PhysRev.107.450

70. N. D. Mermin, Lindhard dielectric function in the relaxation-time approximation. Phys. Rev. B**, 1** (5), 2362-2363 (1970). https://doi.org/10.1103/PhysRevB.1.2362

71. J. Lindhard, On the properties of a gas of charged particles. Kgl. Danske Videnskab. Selskab Mat.-fys. Medd.**, 28** (8), 1-57 (1954).

72. V. Ochkur, The Born-Oppenheimer method in the theory of atomic collisions. J Sov. Phys. JETP**, 18** (2), 503-508 (1964).

73. C. T. Chantler, Detailed tabulation of atomic form factors. Photoelectric absorption and scattering cross section, and mass attenuation coefficients in the vicinity of absorption edges in the soft X-Ray (Z=30–36, Z=60–89, E=0.1 keV–10 keV), addressing convergence issues of earlier work. J. Phys. Chem. Ref. Data**, 29** (4), 597-1056 (2000). https://doi.org/10.1063/1.1321055

74. S. Tanuma, S. Ichimura, K. Goto, et al., Experimental determinations of electron inelastic mean free paths in silver, gold, copper and silicon from electron elastic peak intensity ratios. J. Surf. Anal.**, 9** (3), 285-290 (2002). https://doi.org/10.1384/jsa.9.285

75. H. Kanter, Slow-electron mean free paths in aluminum, silver, and gold. Phys. Rev. B**, 1** (2), 522-536 (1970). https://doi.org/10.1103/PhysRevB.1.522

76. S. M. Sze, J. L. Moll, T. Sugano, Range-energy relation of hot electrons in gold. Solid State Electron.**, 7** (7), 509-523 (1964). https://doi.org/10.1016/0038-1101(64)90088-7

77. H. Shinotsuka, S. Tanuma, C. J. Powell, et al., Calculations of electron inelastic mean free paths. X. Data for 41 elemental solids over the 50 eV to 200 keV range with the relativistic full Penn algorithm. Surf. Interface Anal.**, 47** (9), 871-888 (2015). https://doi.org/10.1002/sia.5789

78. D. R. Penn, Electron mean-free-path calculations using a model dielectric function. Phys. Rev. B**, 35** (2), 482-486 (1987). https://doi.org/10.1103/physrevb.35.482

79. J. C. Ashley, Interaction of low-energy electrons with condensed matter: stopping powers and inelastic mean free paths from optical data. J. Electron. Spectrosc. Relat. Phenom.**, 46** (1), 199-214 (1988). https://doi.org/10.1016/0368-2048(88)80019-7

80. S. Tanuma, C. J. Powell, D. R. Penn, Calculations of electron inelastic mean free paths for 31 materials. Surf. Interface Anal.**, 11** (11), 577-589 (1988). https://doi.org/10.1002/sia.740111107

81. S. T. Perkins, D. E. Cullen, S. M. Seltzer *Tables and graphs of electron-interaction cross sections from 10 eV to 100 GeV derived from the LLNL Evaluated Electron Data Library (EEDL), Z = 1--100*; UCRL-50400-Vol.31; 1991.

82. S. Tanuma, C. J. Powell, D. R. Penn, Calculations of electron inelastic mean free paths. Surf. Interface Anal.s**, 37** (1), 1-14 (2005). https://doi.org/10.1002/sia.1997

83. S. Tanuma, C. J. Powell, D. R. Penn, Calculations of electron inelastic mean free paths. IX. Data for 41 elemental solids over the 50 eV to 30 keV range. Surf. Interface Anal.**, 43** (3), 689-713 (2011). https://doi.org/10.1002/sia.3522

84. V. P. Zhukov, E. V. Chulkov, P. M. Echenique, Lifetimes and inelastic mean free path of low-energy excited electrons in Fe, Ni, Pt, and Au:Ab initio GW+T calculations. Phys. Rev. B**, 73** (12),

125105 (2006). https://doi.org/10.1103/PhysRevB.73.125105

85. M. J. Berger ESTAR, PSTAR, and ASTAR: Computer programs for calculating stopping-power and range tables for electrons, protons, and helium ions (version 1.21),(1999). http://physics.nist.gov/Star, http://physics.nist.gov/Star (Accessed March 31, 2023)..

86. H. T. Nguyen-Truong, Electron inelastic mean free path at energies below 100 eV. J. Phys. Condens. Matter**, 29** (21), 215501 (2017). https://doi.org/10.1088/1361-648X/aa6b9d

87. M. Gryziński, Classical Theory of Atomic Collisions. I. Theory of Inelastic Collisions. Phys. Rev.**, 138** (2A), A336-A358 (1965). https://doi.org/10.1103/PhysRev.138.A336

88. M. Gryziński, Two-particle collisions. II. Coulomb collisions in the laboratory system of coordinates. Phys. Rev.**, 138** (2A), A322-A335 (1965). https://doi.org/10.1103/PhysRev.138.A322

89. Z. J. Ding, X. D. Tang, R. Shimizu, Monte Carlo study of secondary electron emission. J. Appl. Phys.**, 89** (1), 718-726 (2001). https://doi.org/10.1063/1.1331645

90. Z. J. Ding, H. M. Li, X. D. Tang, et al., Monte Carlo simulation of absolute secondary electron yield of Cu. Appl. Phys. A**, 78** (4), 585-587 (2004). https://doi.org/10.1007/s00339-002-1994-3

91. M. Azzolini, M. Angelucci, R. Cimino, et al., Secondary electron emission and yield spectra of metals from Monte Carlo simulations and experiments. J. Phys. Condens. Matter**, 31** (5), 055901 (2018). https://doi.org/10.1088/1361-648x/aaf363

92. D. C. Joy, A database on electron-solid interactions. Scanning**, 17** (5), 270-275 (1995). https://doi.org/10.1002/sca.4950170501

93. D. Hasselkamp, S. Hippler, A. Scharmann, Ion-induced secondary electron spectra from clean metal surfaces. Nucl. Instrum. Methods Phys. Res. B**, 18** (1-6), 561-565 (1986). https://doi.org/10.1016/s0168-583x(86)80088-x

94. S. Tanuma, C. J. Powell, D. R. Penn, Calculations of stopping powers of 100 eV to 30 keV electrons in 10 elemental solids. **37** (11), 978-988 (2005). https://doi.org/10.1002/sia.2092

95. H. Gümüş, Ö. Kabadayi, Practical calculations of stopping powers for intermediate energy electrons in some elemental solids. Vacuum**, 85** (2), 245-252 (2010). https://doi.org/10.1016/j.vacuum.2010.06.004

96. H. Shinotsuka, S. Tanuma, C. J. Powell, et al., Calculations of electron stopping powers for 41 elemental solids over the 50 eV to 30 keV range with the full Penn algorithm. Nucl. Instrum. Methods Phys. Res. B**, 270**, 75-92 (2012). https://doi.org/10.1016/j.nimb.2011.09.016

97. H. T. Nguyen-Truong, Determination of the maximum energy loss for electron stopping power calculations and its effect on backscattering electron yield in Monte-Carlo simulations applying continuous slowing-down approximation. J. Appl. Phys.**, 114** (16), 163513 (2013). https://doi.org/10.1063/1.4827843

98. D. C. Joy, S. Luo, R. Gauvin, et al., Experimental measurements of electron stopping power at low energies. Scanning Microscopy**, 10** (3), 653-666 (1996). https://digitalcommons.usu.edu/micro scopy/vol10/iss3/4